JOURNAL OF CATALYSIS 120, 88–107 (1989)

A Comparative Study on Perovskite-Type Mixed Oxide Catalysts $A'_xA_{1-x}BO_{3-\lambda}$ (A' = Ca, Sr, A = La, B = Mn, Fe, Co) for NH_3 Oxidation

YUE WU,[1] TAO YU, BO-SHENG, DOU, CHENG-XIAN WANG, XIAO-FAN XIE, ZUO-LONG YU, SHU-RONG FAN, ZHI-RONG FAN, AND LIAN-CHI WANG

Changchun Institute of Applied Chemistry, Academia Sinica, Changchun 130022, China

Received November 22, 1988; revised June 2, 1989

Three series of samples having the stoichiometry $A'_xA_{1-x}BO_{3-\lambda}$ (x = 0–1, B = Mn, Fe, Co) were prepared and used as catalysts for NH_3 oxidation. It was found that even at $x = 0$ or $x = 1$ the compositions of the catalysts were nonstoichiometric. The nonstoichiometric amount of oxygen, λ, with which the crystal structure, defects in the solid, reactivity with reactant oxygen, and catalytic activity could be correlated, was a function of x. A single-phase, solid solution exists in the composition range from $x = 0$ to 0.4. A miscibility gap appears at about $A'/A = 1$ ($x = 0.4$) and then an $A'BO_3$ phase is found at $A'/A = 1$. This two-phase region extends until the appearance of the cubic phase at $x = 1.0$. Doping with lower valence cations (A') in the case of ABO_3 results either in an increase in the oxidation state of B or in the formation of oxygen vacancies. In the case of Mn, both λ and the concentration of Mn^{4+} depend linearly upon x, but in the case of Co, due to the instability of Co^{4+} toward reduction by O^{2-}, only λ increases. The case of Fe is situated between the above two. By ED, EM, and Mössbauer investigation, a vacancy-ordering in the ferrite system was observed. XPS, TPD, and EPR measurements gave results suggesting the possibility of the formation of O_2^- or O^-. The adsorbing capacity of catalyst surface to oxygen depends closely on λ. The catalytic activity of $A'_xA_{1-x}BO_{3-\lambda}$ mixed oxides in the NH_3 oxidation in general could be attributed to the extent of the redox reaction

$$2\,B^{4+} + O^{2-} \underset{\text{Mn}}{\overset{\text{Co}}{\rightleftharpoons}} 2\,B^{3+} + \tfrac{1}{2}O_2(g) + \text{Vo}.$$

The Mn and Co systems are just two extreme cases. The dependence of the activity of Fe-containing mixed oxides on their redox potential was confirmed by TPR and ^{18}O-isotopic exchange study.

The mixed oxides which have crystal structures analogous to natural minerals such as perovskite (ABO_3), scheelite (ABO_4), and spinel (AB_2O_4) may be used as model compounds for investigating the role of defects in catalysts; moreover, some of them have been developed into catalysts which have seen application. Therefore, extensive interest in this field has been aroused recently (*1*). There have been papers related to these series of compounds but most of them were generally purely structural (*2*(*a*)) and chemical (*2*(*b*)). Only recent developments in solid state chemistry have correlated physical properties and chemical features with the nature of the defects (*3*). In this paper we introduce our work concerning the perovskite-type catalysts used in NH_3 oxidation. Three series of $A'_xA_{1-x}BO_3$ (A' = Ca or Sr, A = La, B = Mn, Fe, Co) catalysts were prepared by varying x from 0 to 1, since it was found even at $x = 0$ or 1 that the composition of catalysts in each series would be nonstoichiometric. The nonstoichiometric amount of oxygen (λ) was a function of x. The activity of catalysts could be attributed to the nonstoichiometric amount of oxygen λ and explained by the presence of different defects.

[1] To whom correspondence should be addressed.

0021-9517/89 $3.00

I. EXPERIMENTAL

1. Catalyst Preparation and Catalytic Activity Measurement

Samples were prepared by mixing nitrate solutions of Mn (or Fe, Co), La, and Ca (or Sr) according to defined composition, precipitation with NH_4OH + NH_4HCO_3, followed by thermal decomposition and calcination of the precipitates.

Activity of the catalysts for ammonia oxidation was measured in a conventional flow system using 10 ml of catalyst and a feed composition of NH_3/air at 1/9 by volume. The quantities of NH_3 and NO in the product steam were determined by conventional acid–base titration. The conversion of NH_3 in all cases was complete; therefore the selectivity of NO under the same conditions was taken as catalytic activity for comparison.

2. Oxygen Determination

(*1*) *Nonstoichiometric amount of oxygen* (λ). A known mass of sample was dried after 120°C and dissolved in hydrochloric acid. La^{3+}, Ca^{2+} (or Sr^{2+}), and Mn^{3+} (Fe^{3+} or Co^{3+}) ions were separated through an ion exchange column and then determined by titration with EDTA. Mn^{4+} and Mn^{3+} were determined by Brists' method. The content of Fe^{3+} was determined by titrating with $K_2Cr_2O_4$ in HCl (3 *N*) with an excess of Mohr' salt. Co^{3+} was analyzed quantitatively by iodometry. The data obtained were then used to calculate the nonstoichiometric amount of oxygen in the samples.

(*2*) *Surface excess oxygen.* The KI method was used (*4*).

(*3*) *Adsorbed oxygen.* Measurements were carried out either on an ordinary high vacuum apparatus volumetrically or by TPD. Samples were degassed at 10^{-5} Torr at 600°C for 2 h, and then the amounts of adsorbed oxygen were determined at different temperatures.

(*4*) *Surface oxygen state.* X-ray photoelectron spectrometry (an NP-1 spectrometer or a SHIMADZU ESCA 650B spectrometer) was used with Mg$K\alpha$ (1253.6 eV) as the X-ray source. The resolution for Ag 3*d* peak was 1.02 eV. Other parameters were signal–background ratio, 16.8 : 1; count speed, 275,039 c/s; and vacuum chamber pressure, 2.2×10^{-8} Torr.

(*5*) *Reducibility of catalyst.* Measurements were carried out by TPR using an apparatus similar to that described by Cvetanovic and Amenomiya for a TPD study (*5*).

(*6*) *Isotopic exchange.* ^{18}O exchange between O_2 in the gas phase and O_2 in the catalyst was conducted in a closed circulation system prior to the reaction; the sample was treated with purified $^{16}O_2$ circulating at 400°C and subsequently evacuated at 350°C. O_2 enriched in ^{18}O was prepared by mixing $^{18}O_2$ and pure $^{16}O_2$. ^{18}O distribution in gaseous oxygen was analyzed with a mass spectrometer after intermittent sampling.

3. Catalyst Characterization

(*1*) *Crystal structure.* X-ray diffractograms for powdered samples of the Mn- or Co-containing series were recorded on a Shimadzu automatic recording X-ray diffractometer (Type VD-1A) operating at 40 kV with a working current of 10 mA using Cu$K\alpha$ radiation in combination with a nickel filter.

In order to investigate the crystal grain size and crystal distortion, measurements for the Fe system were carried out on a Rigaku diffractometer (Type D/MAX-rA) operating at 40 kV and 200 mA using Cu$K\alpha$ radiation filtered with a graphite monochromator. X-ray diffractograms were recorded with a Geiger counter during stepped scans.

(*2*) *Valence states of the surface metal ions.* ESR measurements were carried out using a conventional ESR spectrometer with 975 kHz field modulation. The instrument operated at a frequency of 9149 MHz (determined with a cavity wavemeter). Unless otherwise stated, experiments were performed at 25°C.

A homemade, constant acceleration spectrometer was used for Mössbauer spectroscopy. The source was a 25 mCi sample of ^{57}Co (Pd). The thickness of specimen corresponded to 50 mg/cm^2. The velocity scale was calibrated with the spectrum of sodium nitroprusside.

(*3*) *Physico-chemical properties.* Thermodifferential and thermogravimetric analyses were carried out with a Rigaku thermoanalysis apparatus under the following conditions: sample, 100 mg; heating rate, 10°C/min; air flow rate, 50 ml/min; temperature range, 20–800°C.

A simple air adsorption method was used to measure the surface areas.

The SEM investigations were performed with a JXA-840 Jeol scanning electron microscope.

II. EXPERIMENTAL RESULTS AND DISCUSSION

Defect types and concentrations in metal oxides can be regulated in wide ranges by doping with foreign ions and by changing the conditions of preparation and treatment. For instance, Kamata *et al.* (*6*) prepared samples of $LaMnO_3$ under different oxygen partial pressures in which the value of λ varied from -0.053 to $+0.079$. By substituting La with Ca (doping), we obtained a series of catalysts containing various nonstoichiometric amounts of oxygen with λ ranging from -0.059 to $+0.110$.

Similar relations between x and λ were observed for all three series of mixed oxides. Their catalytic activity and other properties varied markedly with the nonstoichiometric amount of oxygen (λ) in the samples (Tables 1a–c).

The process of preparing these series of perovskite-type mixed oxides, with $Ca_xLa_{1-x}MnO_3$ as an example, can be expressed by the equation

$$x\mathrm{CaCO_3} + \tfrac{1}{2}(1-x)\mathrm{La_2(CO_3)_3} + \mathrm{MnCO_3} \xrightarrow{600\text{–}900^\circ\mathrm{C}} x\mathrm{CaO}\cdot\tfrac{1}{2}(1-x)\mathrm{La_2O_3}\cdot\mathrm{MnO} \xrightarrow{\Delta} \mathrm{Ca_xLa_{1-x}MnO_3}.$$

In the course of preparation, the change of valence state of the manganese ion with calcination temperatures has been traced by detecting the Mn^{2+} and Mn^{4+}–O–Mn^{3+} ESR signals for the sample with $x = 0.8$. The results are shown in Fig. 1. Mn^{2+} signals in the raw material carbonate decreased gradually with increasing calcination temperatures and disappeared completely when the temperature was raised to 600–700°C. A sample for Mn^{4+}–O–Mn^{3+} double exchange appeared at 700°C,

TABLE 1a

Composition, Structure, and Physico-Chemical Properties of Catalysts $Ca_xLa_{1-x}MnO_3$

x-Value	$Ca_xLa_{1-x}MnO_3$	S (m^2/g)	Mn^{4+}/Mn (%)	Cryst. parameter (Å)	Surf. excess O_2 (ml/m^2 × 10)	Ads. O_2 at 600°C (ml/m^2 × 10)		NO select. at 800°C (%)
						Rev.	Irrev.	
0.0	$LaMnO_{3.110}$	4.31	21.95	$a = 5.33$ $b = 5.79$ $c = 8.05$	1.6	4.25	3.87	90.0
0.3	$Ca_{0.3}La_{0.7}MnO_{3.056}$	4.79	41.17	$a = 7.62$	2.2	1.70	1.19	92.4
0.5	$Ca_{0.5}La_{0.5}MnO_{3.026}$	5.79	55.23	$a = 7.60$	2.5	0.31	2.04	93.7
0.7	$Ca_{0.7}La_{0.3}MnO_{3.014}$	6.22	72.82	$a = 7.59$	3.5	0.50	5.29	96.5
0.8	$Ca_{0.8}La_{0.2}MnO_{2.97}$	5.18	79.30	$a = 7.47$	4.4	0.66	11.14	97.7
0.9	$Ca_{0.9}La_{0.1}MnO_{2.97}$	5.17	89.33	$a = 7.45$	4.5	0.68	15.07	97.8
1.0	$CaMnO_{2.14}$	3.31	88.14	$a = 7.42$	6.8	1.51	28.94	97.4

TABLE 1b

Composition, Structure, and Physico-Chemical Properties of Catalysts $Sr_xLa_{1-x}CaO_3$

x-Value	$Sr_xLa_{1-x}CoO_3$	S (m^2/g)	Co^{4+}/Co (%)	Cryst. sys.	Ads. O_2 at 200–700°C (ml/g)	NO selec. at 700°C (%)
0.0	$LaCoO_{2.955}$	3.25	9.06	R[a]	0.0	97.0
0.1	$Sr_{0.09}La_{0.91}CoO_{2.986}$	2.65	8.39	R	0.035	98.8
0.2	$Sr_{0.22}La_{0.78}CoO_{2.843}$	3.08	9.50	R	0.176	98.6
0.4	$Sr_{0.42}La_{0.68}CoO_{2.80}$	2.22	7.40	R		98.1
0.5	$Sr_{0.46}La_{0.54}CoO_{2.79}$	2.82	7.78	R	0.640	98.0
0.6	$Sr_{0.60}La_{0.40}CoO_{2.77}$	3.65	12.97	C[b]		96.4
0.8	$Sr_{0.84}La_{0.16}CoO_{2.639}$	0.65	15.02	C	0.770	94.7
1.0	$SrCoO_{2.611}$	0.68	21.94	C	0.800	86.0

[a] R, rhombohedral.
[b] C, cubic.

strengthened with increasing temperature, and finally reached a maximum intensity at 1000°C (Fig. 2). It may thus be concluded that the perovskite-type manganate would be formed by calcining at 1000°C for 4 h. The results of X-ray diffraction study for this series of samples have also shown that the whole series have mainly the same perovskite-like crystal structure, as discussed in the following section.

Based on the experimental results, exploratory discussion will be given below for the course of defect formation, the types of defect in such catalysts, and the role of defects in the catalytic reaction.

1. Crystal Structure of Perovskite-Like Mixed Oxides

The crystal structure of perovskite, ABO_3, is well known: the A ion is coordinated by 12 oxygen ions which in turn belong to eight BO_6 octahedron sharing corners. When doped with foreign ions the lattice either can form an ideal cubic perovskite structure or can distort significantly from the cubic phase to form a te-

TABLE 1c

Composition, Structure, and Physico-Chemical Properties of Catalysts $Sr_xLa_{1-x}FeO_3$

x-Value	$Sr_xLa_{1-x}FeO_3$	S (m^2/g)	Fe^{4+}/Fe (%)	Cryst. sys.	Ads. O_2 at 600°C (ml/m^2)	NO select. at 800°C (%)
0.0	$LaFe_{0.96}O_{2.94}$	1.73		O[a]	0.69	88.3
0.1	$Sr_{0.1}La_{0.9}FeO_{2.993}$	1.70	8.6	O	0.77	91.8
0.2	$Sr_{0.2}La_{0.8}FeO_{2.982}$	2.40	16.5	O	2.44	95.3
0.4	$Sr_{0.4}La_{0.6}FeO_{2.954}$	3.00	30.8	O	2.11	96.9
0.5	$Sr_{0.5}La_{0.5}FeO_{2.934}$	3.04	36.8	O + C	1.89	95.0
0.7	$Sr_{0.7}La_{0.3}FeO_{2.924}$	5.81	54.8	O + C	1.14	95.6
0.9	$Sr_{0.9}La_{0.1}FeO_{2.865}$	2.00	63.0	O + C	5.23	92.2
1.0	$SrFeO_{2.830}$	0.73	66.0	C[b]	13.70	93.6

[a] O, orthorhombic.
[b] C, cubic.

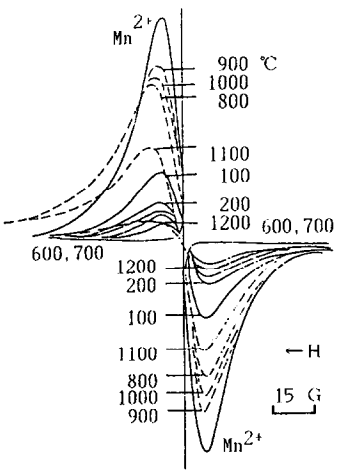

FIG. 1. Change in the ESR signal of different Mn ions in samples $Ca_{0.8}La_{0.2}MnO_3$ with calcination temperature (— Mn^{2+}; --- Mn^{3+}–O–Mn^{4+}).

tragonal, orthohombic, or rhombohedral phase. Recently, some authors have reported (*2(a)*) that at a higher concentration of defects, nonstoichiometry generally leads to an ordering of the defects. The network could thus be rearranged, for example, to a Brownmillerite-like structure $ABO_{2.5}$ which can be considered as an oxygen-deficient perovskite ABO_3 corresponding to $\lambda = 0.5$.

X-ray diffraction (XRD) patterns for different series are given in Fig. 3a–c and some of the lattice parameters are reported in Table 1. For lower x-substitution ($x < 0.4$) they reveal a slight rhombohedral or orthorhombic distortion with the structure ABO_3. With an increase in x up to ~0.8, a cubic symmetry phase of $A'BO_3$ was found in addition to the major perovskite phase. The XRD phase analysis indicates only the presence of the cubic phase of $A'BO_3$ at $x = 1$. Those results are consistent with almost all reported in the literature (*7*). It can be seen that a single-phase, solid solution exists in the composition range from $x = 0$ to 0.4, wherein ions A and A' are randomly substituted. A miscibility gap appears at about $A'/A = \frac{2}{3}$ ($x = 0.4$), and then the $A'BO_3$ phase is found at $A'/A = 1$ ($x = 0.5$) in addition to $A'_xA_{1-x}BO_3$. This two-phase region is continuous until the appearance of the cubic phase with $x = 1.0$.

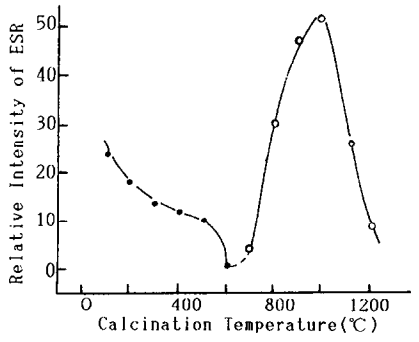

FIG. 2. Dependence of intensities of ESR signals of Mn ions in samples $Ca_{0.8}La_{0.2}MnO_3$ on calcination temperature (●—Mn^{2+}; ○—Mn^{3+}–O–Mn^{4+}).

Furthermore, our results showed that the peaks of XRD become wider for an A'-substituted sample in the single-phase region (e.g., $x = 0$–0.4 in $Sr_xLa_{1-x}FeO_3$) at the same calcination temperature but narrower with increasing calcination temperature (e.g., $Sr_{0.4}La_{0.5}FeO_3$). Crystallite sizes and lattice distortions for these samples were calculated from the relation

$$(2\omega)^2 \cos^2 \theta_0 = (4/\pi^2) \cdot (\lambda/D) + 32\langle\varepsilon^2\rangle \sin^2 \theta_0, \quad (2)$$

where θ_0 is the corresponding Bragg angle, D is the average thickness of the crystal perpendicular to plane $[h\ k\ l]$, and $\langle\varepsilon^2\rangle$ is the square of the average lattice distortion of the polycrystal perpendicular to plane $[h\ k\ l]$. The results are given in Table 2. It can be seen from these results that lattice distor-

TABLE 2

Average Size of Polycrystal and Lattice Distortion

Sample	D_{101} (Å)	$\langle\varepsilon^2\rangle_{101}$
1. $LaFe_{0.96}O_{2.94}$	790	1.0×10^{-3}
2. $Sr_{0.1}La_{0.9}FeO_{2.993}$	1200	1.1×10^{-3}
3. $Sr_{0.2}La_{0.8}FeO_{2.982}$	390	2.1×10^{-3}
4. $Sr_{0.4}La_{0.6}FeO_{3-\lambda}$		
1000°C	190	4.9×10^{-3}
1100°C	230	1.1×10^{-3}
1200°C	400	0.8×10^{-3}

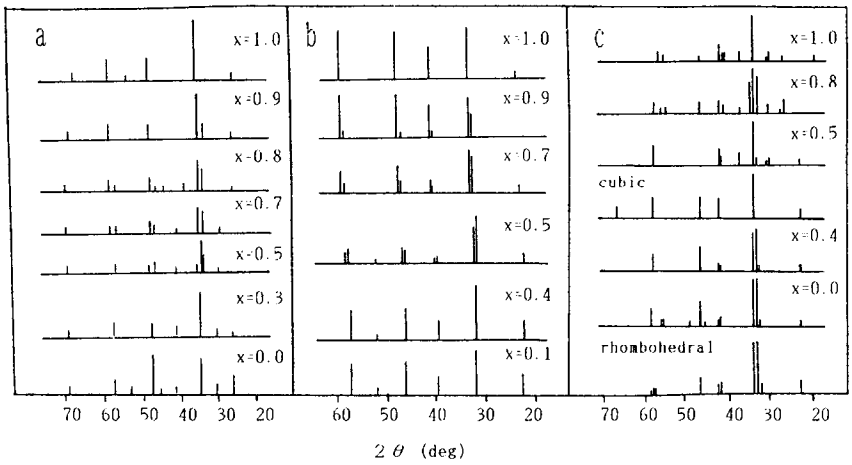

FIG. 3. X-ray diffraction patterns for (a) $Ca_xLa_{1-x}MnO_3$, (b) $Sr_xLa_{1-x}FeO_3$, and (c) $Sr_xLa_{1-x}CoO_3$.

tion increased monotonically with the amount of *A* which had been substituted. The calcination temperature exerts the reverse effect. Results obtained from SEM support these conclusions as shown in Fig. 4. The smallest particles and the best distribution of them are given by the samples containing the most Sr, but the largest particles and sintering are observed from the sample calcined at highest temperature.

2. *Defects formed in* $A'_xA_{1-x}BO_3$

Now suppose the exposed surface consists of [100] planes, which are the stable planes in the perovskite structure due to the square array of Mn–O–Mn (*8*). A perfectly stoichiometric perovskite, i.e., ABO_3, can be illustrated with a defect structure diagram as shown in Fig. 5a–d. Variation in *x*-values corresponds to doping with foreign ions of lower valence, i.e., *A'* (Ca^{2+} or Sr^{2+}) in the case of ABO_3. According to the principle of electroneutrality, doping with lower-valence cations either increase the oxidation state of *B* (Fig. 5b) or decrease the number of oxygen anions in the lattice (Fig. 5c), or both (Fig. 5d). The defect reaction may be represented by the equations

$$A'_xA_{1-x}B^{3+}_{1-x}B^{4+}_xO_3 \rightarrow ABO_3 + xA|A'|' + xB^{3+}|B^{4+}|^{\cdot} \quad (3)$$

or

$$A'_xA_{1-x}Vo_\lambda B^{3+}O_{3-\lambda} \rightarrow ABO_3 + xA|A'|' + \lambda|O|^{\cdot\cdot} \quad \left(\lambda = \frac{x}{2}\right). \quad (4)$$

Moreover, in the case of $LaMnO_3$ it has been found that at lower Ca-substitution, λ is positive, showing that oxygen anions are in excess in the crystal. But due to its relatively large radius, the oxygen ion could not exist in such a lattice as an interstitial anion. Therefore a certain number of metal ions must be missing from the lattice, forming cation vacancies $|K|^{n'}$ (□). Because of the stabilizing action of BO_6 octahedra in the perovskite structure, no *B* cation vacancies have been found in these compounds, only *A* cation vacancies (*9*). For $LaMnO_3$ (Fig. 6a), only a La cation vacancy was found (*6*). From electroneutrality, the presence of one $|La|'''$ vacancy can correspondingly give rise to a change of valence state of three neighboring Mn^{3+} to Mn^{4+} (Fig. 6b). With this scheme it is understandable why the Mn^{4+} content in $LaMnO_{3.110}$ (21%, the same as in (*10*)) far exceeds the stoichiometric value (0% in $LaMnO_3$).

The high-valence Mn^{4+} ion can be regarded as a Mn^{3+} ion associated with a monocharged positive hole $|e|^{\cdot}$, i.e., $Mn^{4+} = Mn^{3+} \cdot |e|^{\cdot}$. The bound defect electron

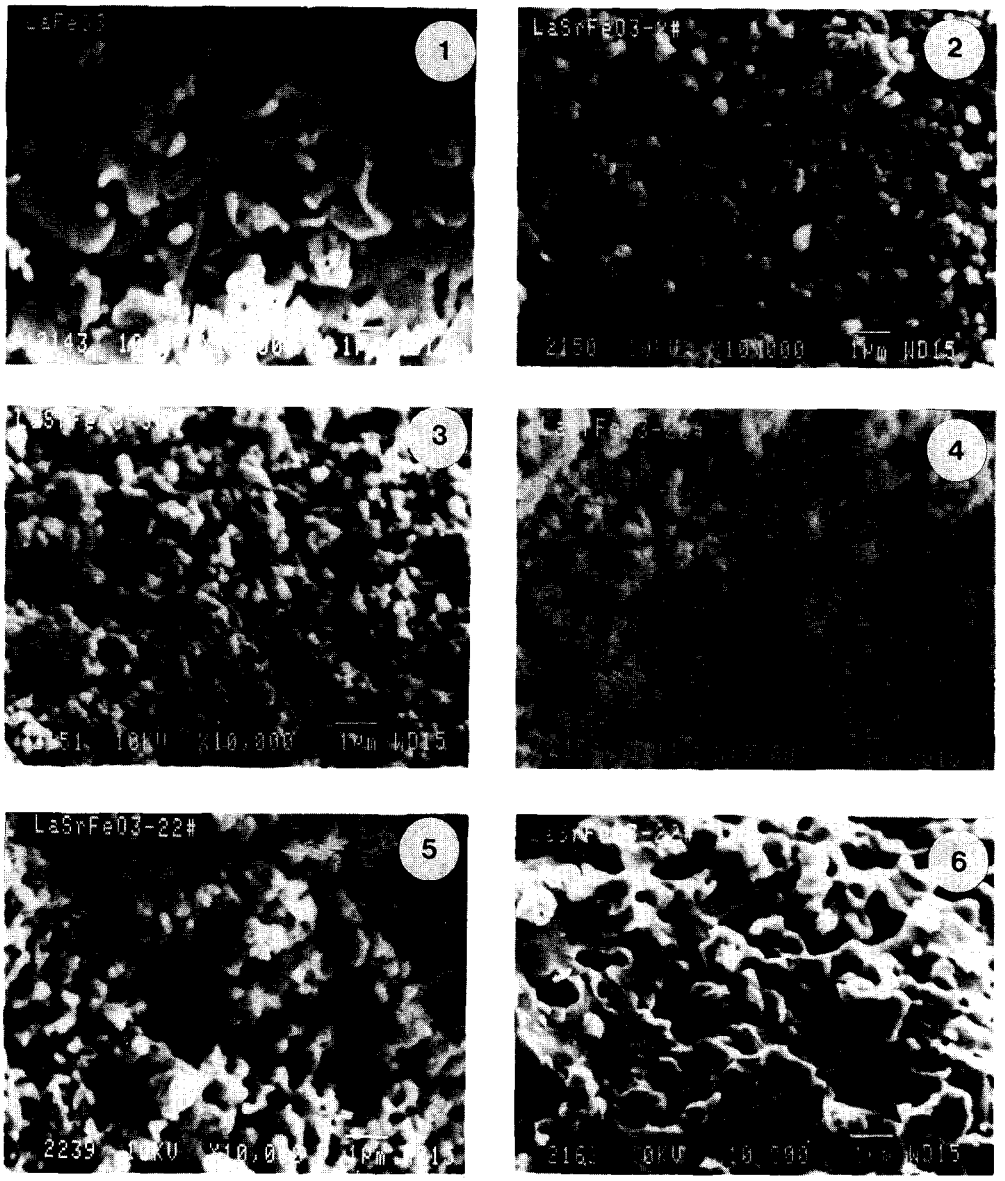

FIG. 4. SEM photographs (numbers correspond to those in Table 2).

can split from $Mn^{3+} \cdot |e|^{\cdot}$ freely and form a quasi-free hole. Accordingly, the equation from the formation of this defect site should be written in the form

$$LaMnO_{3+\lambda} = LaMnO_3 + \frac{2\lambda}{3}|La|''' + 2\lambda|e|^{\cdot} + \frac{\lambda}{3}La_2O_3. \quad (5)$$

Doping with lower valence cations, e.g., Ca^{2+}, would decrease the number of O^{2-} in the lattice. To satisfy electroneutrality, if an O^{2-} vacancy is present, a defect $|O|^{\cdot\cdot}$ usually binds the free electron e′ (ⓔ), an F-center, and causes a neighboring high-valence metal ion to become lower valence (Fig. 6c). The defect reaction may thus be represented by the equation

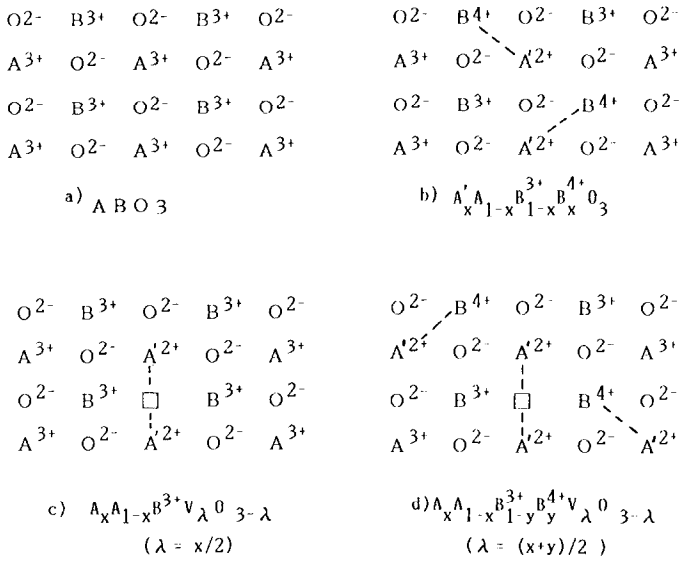

FIG. 5. Defect patterns in $A'_xA_{1-x}BO_3$.

$$Ca_xLa_{1-x}MnO_{(3+\lambda)-\delta} \rightarrow LaMnO_{3+\lambda} + x\ La|Ca|' + \delta|O|^{\cdot\cdot} + (2\delta - x)e'. \quad (6)$$

The measured stoichiometries as well as the B^{4+}/B ratios shown in Tables 1(a)–(c) confirm that our experimental results for all series of samples are consistent with these arguments. The plot of nonstoichiometry (λ) and concentration of B^{4+} as a function of x shown in Fig. 7. The same relationship for the three series has been obtained: in general, both λ and B^{4+} change with x, but there exist differences between them. In the case of Mn, both nonstoichiometry (λ) and concentration of Mn^{4+} in the bulk are linearly dependent on x. It seems that both of the defect reactions, (3) and (4), take place; but in the case of Co, the concentration of Co^{4+} rises from $x = 0.6$ to $x = 1.0$, so probably only reaction (4) takes place, at least in the lower ranges of x. The change of Co^{4+} vs x could also be attributed to the instability of Co^{4+}, which is easily reduced by oxygen released during oxygen vacancy formation. The case of Fe is situated right between the above two cases. The content of oxygen vacancies in samples with lower x is higher than that of Fe^{4+}, but in samples with higher x, the opposite result is obtained. The order of instability of $Mn^{4+} < Fe^{4+} < Co^{4+}$ in air appears to account for these results.

For small defect concentration an interpretation based on statistical thermody-

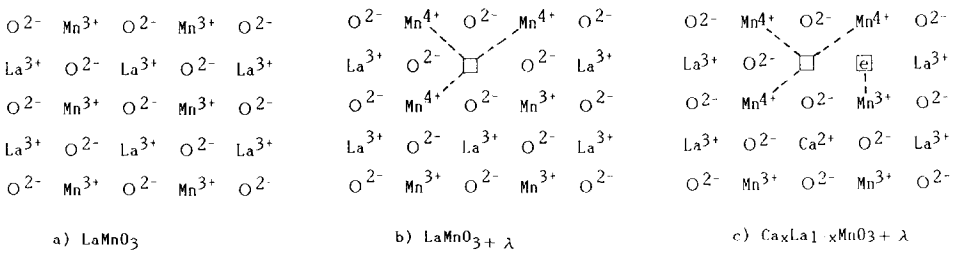

FIG. 6. Defect patterns in $Ca_xLa_{1-x}MnO_3$ samples.

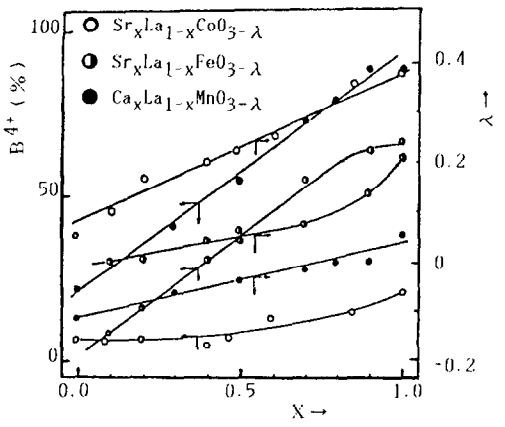

FIG. 7. Relationships among x, λ, and B^{4+} content for $A'_xA_{1-x}BO_3$.

TABLE 3

Chemical Composition of $A'ABO_3$ Obtained by Measurement of the O_2 Released

x-Value	Weight of samples (mg)	Heated to 800°C in flowing air	
		Net loss in weight	$Sr_xLa_{1-x}FeO_3$
0.0	81.25	0.3	$LaFe_{0.91}O_{2.88}$
0.1	81.78	0.3	$Sr_{0.1}La_{0.9}FeO_{2.939}$
0.2	79.88	0.50	$Sr_{0.2}La_{0.8}FeO_{2.891}$
0.4	81.55	0.75	$Sr_{0.4}La_{0.6}FeO_{2.827}$
0.5	80.33	1.10	$Sr_{0.5}La_{0.5}FeO_{2.749}$
0.7	82.27	1.60	$Sr_{0.7}La_{0.3}FeO_{2.674}$
0.9	82.52	2.0	$Sr_{0.9}La_{0.1}FeO_{2.57}$
1.0	81.21	1.8	$SrFeO_{2.569}$

namics, i.e., the point defects as being randomly distributed in the lattice without interaction, has been used to elucidate the mechanism of reactions carried out on or in the solid state, including the catalytic reactions (*1, 11*). At higher concentrations clusters or microdomains may be observed. In some cases, even "shear planes" occur due to segregation of defects. If long range ordering occurs, new compounds with definite composition and structure can be obtained. The implication is that variation of structure with stoichiometry should, to a certain extent, exert some influence upon the mixed oxides to change their catalytic properties. Up to now very few authors have dealt with vacancy ordering in mixed oxides, especially to correlate it with catalytic properties.

Of all these systems ferrites seem to be the most extensively investigated phase because the local environment and the oxidation state of iron can be determined by Mössbauer spectroscopy. With the help of this method, in addition to other, classical physical techniques, the existence of vacancy ordering could be elucidated. In the following, we attempt to study more carefully the vacancy ordering in this series of samples and to correlate it with catalytic behavior.

TPD measurements and TG analyses for these series of samples showed that the amount of O_2 released in the temperature range from room temperature up to 500°C was negligible. At higher temperatures, a relatively large amount of O_2 was released (cf. Fig. 8). Although the amount of O_2 released was dependent upon the value of x, by recalculation of the composition of these mixed oxides in consideration of the amount of O_2 released a new nonstoichiometry for each sample could be thus obtained. From the data shown in Table 3, it may be concluded that for lower x the vacancies are apparently disordered by reason of small variation of nonstoichiometry. At higher x, the larger variation of the nonstoichiometry might lead to an ordering of the defects.

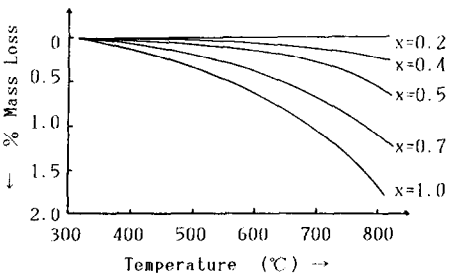

FIG. 8. Percentage mass loss versus temperature for $Sr_xLa_{1-x}FeO_3$.

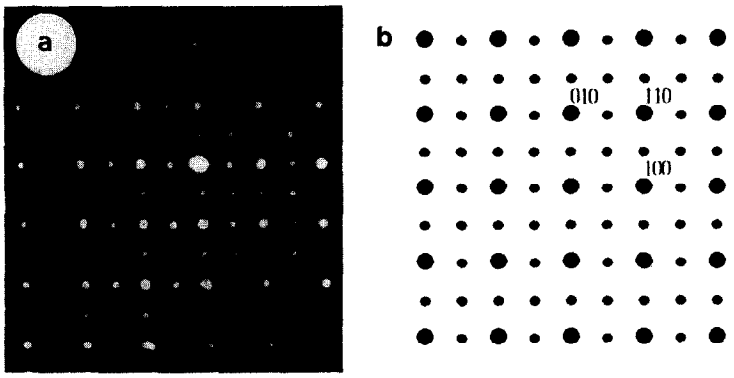

FIG. 9. (a) Electron diffraction pattern of sample $x = 0$ along [001]c showing the doubling of the perovskite cell in both a and b directions. (b) Zone axis [001]c shown schematically.

The absence of superstructure lines in the X-ray diffraction patterns suggests that any periodic ordering takes place to give only small ordered domains. For this reason we carried out ED and EM measurements with the aim of observing superstructure spots indicating some kinds of periodic ordering on a small scale.

Electron diffraction from samples with $x = 0$ gave patterns that at first sight could be indexed in a double perovskite unit cell. Figure 9a shows an example along the [001]c axis, schematically shown in Fig. 9b. From the ED patterns, it could be seen that no superstructure spots were present. Only the basic spots corresponding to the cubic perovskite cell were observed (unit cell, $a_c \times a_c \times a_c$). Electron microscopy of an area of the crystal (Fig. 10) reveals the 3.68- to 3.85-Å lattice fringes of the perovskite planes, but it also shows that the sample corresponds actually to a multitwinned crystal. It is worth pointing out that the distortion is not obvious in powder X-ray diffraction patterns or in electron diffraction patterns, probably because this orthorhombic distortion is relatively small.

These negative results in looking for superstructure spots indicate that (1) the anionic vacancies are randomly distributed, or (2) if some ordering existed it would be nonperiodic, forming clusters of different dimensionalities. We observed that for the composition $x = 0$ the perovskite-type phase predominated but contained intergrowths and dislocations.

Upon the introduction of more Sr^{2+} into $LaFeO_3$ ($x > 0.4$), relatively broad peaks corresponding to a simple cubic subcell were observed in the X-ray diffraction patterns. From ED and EM measurements, the real situation appeared much more complex. In $Ca_xLa_{1-x}FeO_{3-\lambda}$, Vallet-Regi *et al.* (*12*) pointed out that two types of solids, $Ca_2LaFe_3O_8$ (G-type) and $Ca_2Fe_2O_5$ (Brownmillerite-type), were observed to exist. They were both formed by disordered intergrowth. Microscopic examination of the sample with $x = 0.4$ (Fig. 11) reveals a crystal structure which is almost ordered. However, instead of equidistant fringes a more complicated image with a period of 8.0 Å was observed (d_{010}, spacing in Fig. 11). This can be correlated with a hypothetical structure of the compound, as stated in the following paragraph, which would correspond to an ordered sequence of $ABO_{2.75}$ structures. An alternating sequence of two kinds of black lines reflects the presence of both octahedral and tetrahedral environments in the $ABO_{2.75}$ structure.

Figure 12 shows the electron diffraction patterns of the sample with composition $x = 1$. These could be indexed in an $ABO_{2.75}$ unit cell. The corresponding electron micrograph, Fig. 13, shows that the crystal is

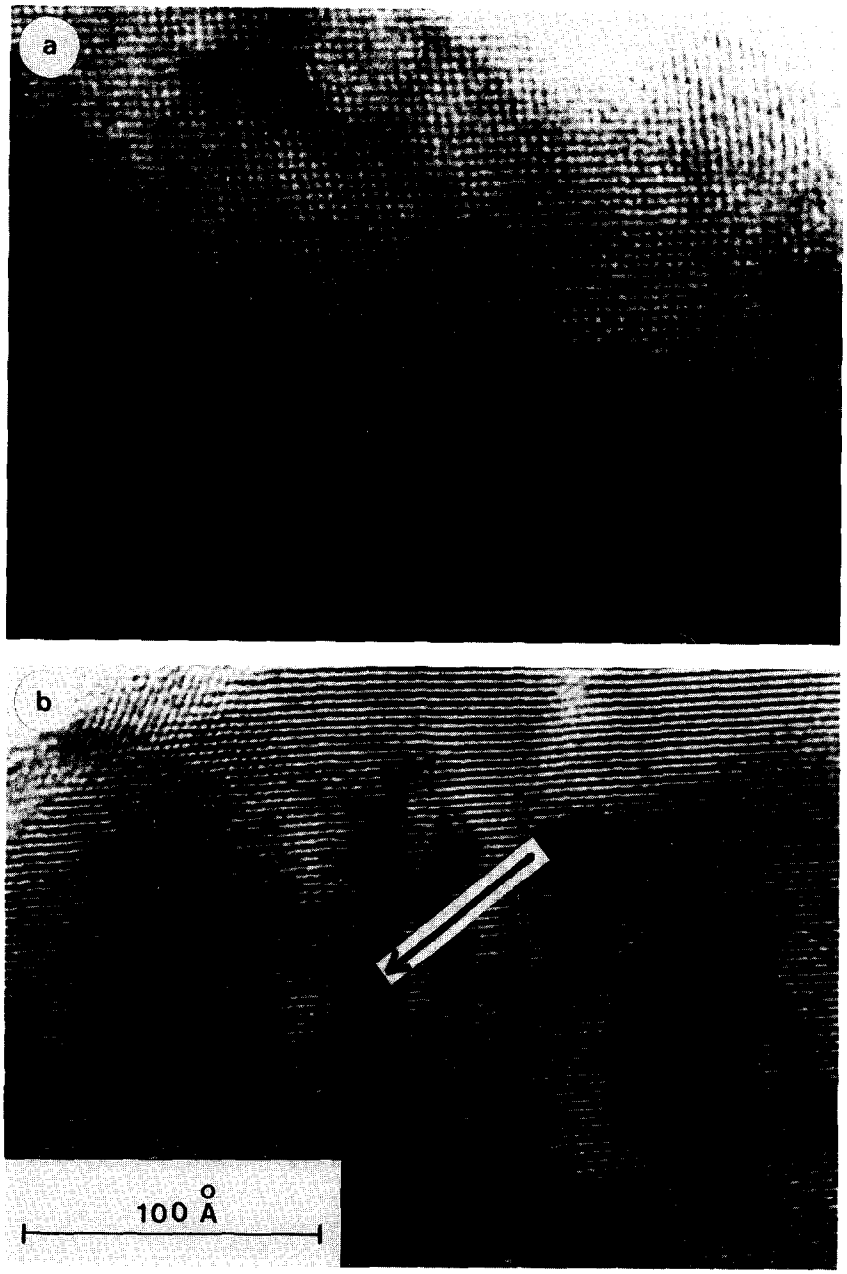

FIG. 10. Electron micrograph showing (a) multitwinning, intergrowth as well as (b) dislocation in the sample $x = 0$.

formed by an ordered region characterized by a spacing of ~8.0 Å ($2a_c$) = d_{010} of the $ABO_{2.75}$ type structure (*13*), a model of which is given in Fig. 13b.

A high resolution structural image of the $ABO_{2.75}$ type region (Fig. 14) shows that the octahedral and the tetrahedral sites alternate along the *b* axis. Moreover, multitwinned crystals were observed.

Recently, based on studies by thermal analysis, optical and electron microscopy, and X-ray diffraction, Reller and Bun-

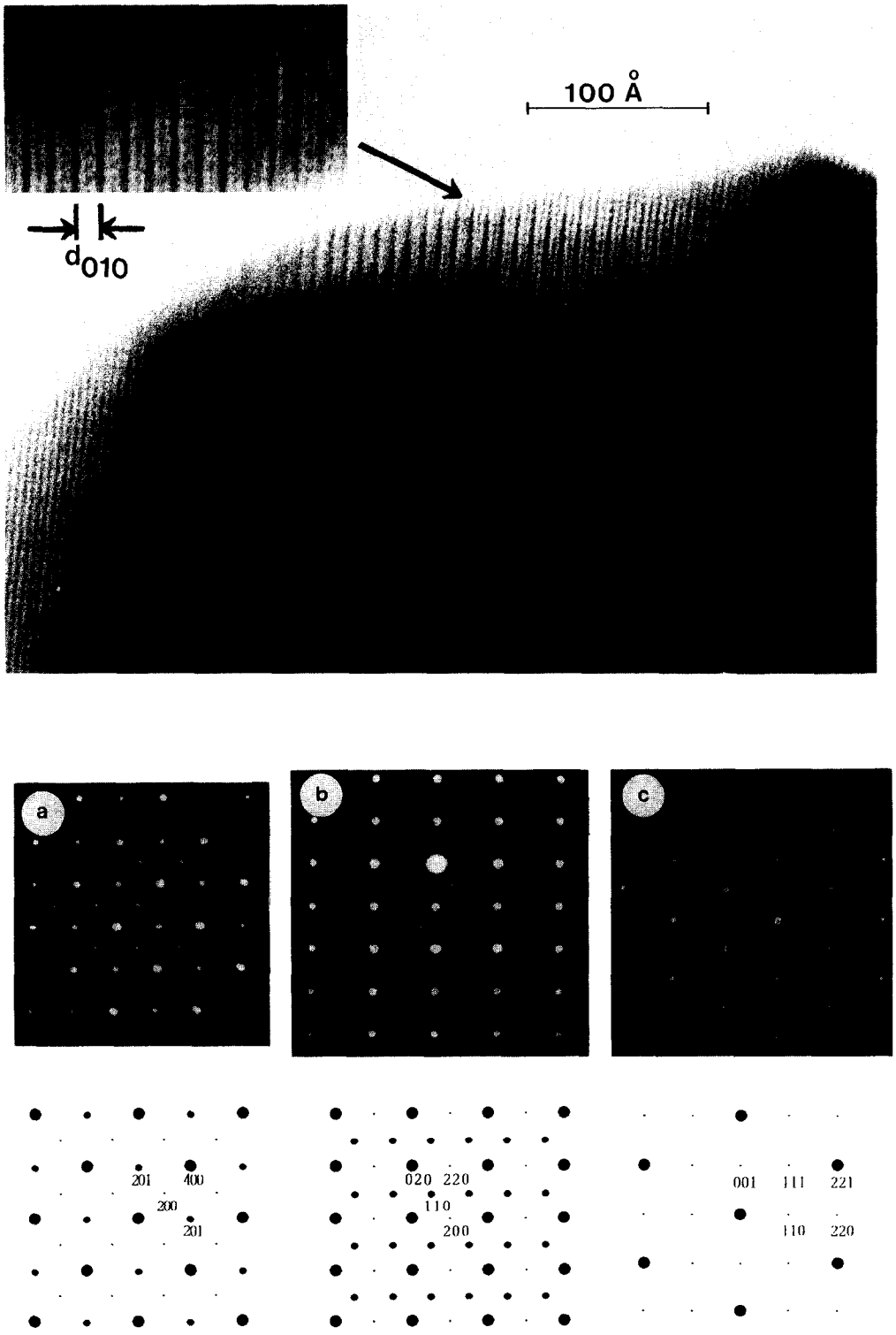

FIG. 12. Electron diffraction patterns corresponding to sample $x = 1.0$ in which zone axes are (a) [010], (b) [101], and (c) [111].

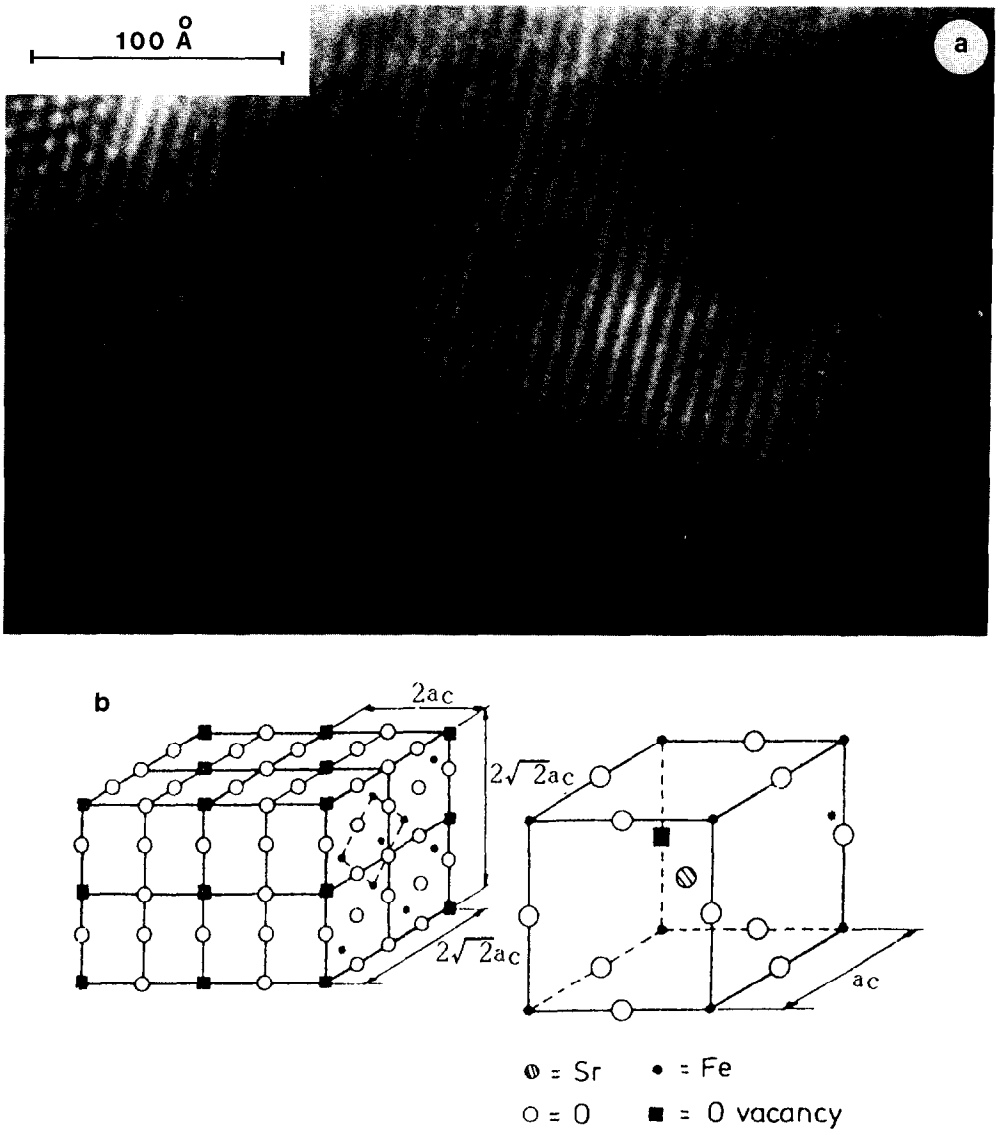

FIG. 13. (a) Image corresponding to the patterns shown in Fig. 12. (b) Model for the oxygen vacancy ordering in $SrFeO_{2.75}$.

senges (*14*) pointed out this kind of structural reaction mechanism as well as concomitant compositional change of reversible reduction/reoxidation processes of perovskite metal oxides might play an important role when these mixed oxides are used as catalysts for oxidation processes.

When account is taken of the results obtained from ED and EM, Mössbauer spectroscopy (MS) can help to elucidate the presence of a certain vacancy ordering. Mössbauer spectra at room temperature were recorded for the representative samples of the $Sr_xLa_{1-x}FeO_{3-\lambda}$. Figure 15 shows some spectra in both paramagnetic and magnetically ordered regimes. Parameters for each component peak are summarized in Table 4.

At room temperature, the MS of the three compounds with $x = 0.0, 0.1, 0.2$

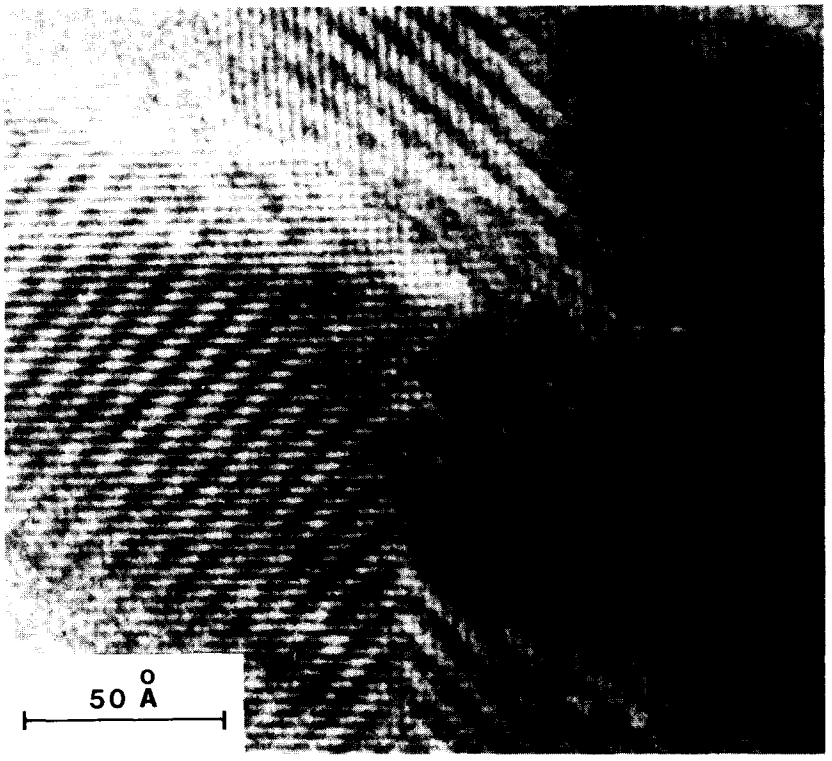

FIG. 14. Structure image of the $SrFeO_{2.75}$ type regions.

show a 6-line spectrum characteristic of the nuclear Zeeman effect. These compounds are antiferromagnetic and the local field at the nuclei is very high ($H_{int} \approx 515$ kOe) despite low bulk magnetization due to opposite orientation of neighboring Fe spins. As more Sr is substituted for La (see Fig. 16) a dramatic change occurs in the MS some-

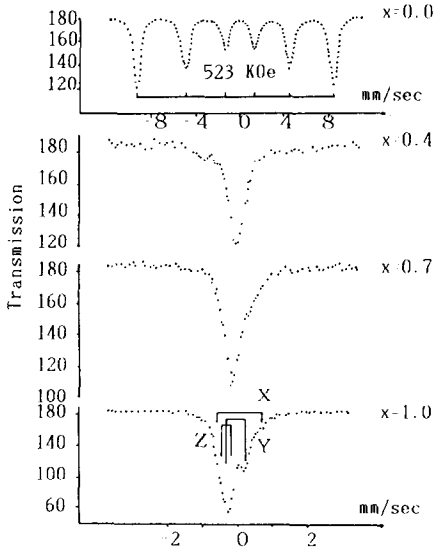

FIG. 15. Mössbauer spectra of several representative catalysts at room temperature.

TABLE 4

Mössbauer Parameters of $Sr_xLa_{1-x}FeO_3$ at Room Temperature

Composition	H_{int} (kOe)	Isomer shift (mm/s)
$LaFe_{2.96}O_{2.94}$	523	0.34
$Sr_{0.1}La_{0.9}FeO_{2.93}$	513	0.32
$Sr_{0.2}La_{0.8}FeO_{2.82}$	507	0.25
$Sr_{0.4}La_{0.6}FeO_{2.54}$		−0.04
$Sr_{0.5}La_{0.5}FeO_{2.934}$		−0.08
$Sr_{0.7}La_{0.3}FeO_{2.924}$		−0.12(L)
		−0.28(R)
$Sr_{0.9}La_{0.1}FeO_{2.865}$		−0.12(L)
		0.24(R)
$SrFeO_{2.83}$		−0.20(L)
		0.28(R)

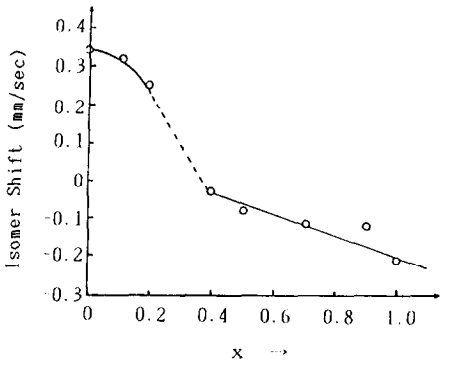

FIG. 16. Isomer shift versus Sr concentration.

where between $x = 0.4$ and 0.5. The 6-line spectrum still recognizable at $x = 0.4$ degenerates into a single-line spectrum at $x = 0.5$ due to a transition from antiferromagnetic (or ferromagnetic) to paramagnetic behavior in which both the local magnetic field and the nuclear Zeeman splitting vanish. Samples with Sr concentrations of $x = 0.7$, 0.9, and 1.0 display small peaks on the positive velocity slope of the prominent line.

The room temperature isomer shifts (IS) of the series $Sr_xLa_{1-x}FeO_{3-\lambda}$ drop drastically in the samples with $0.0 \leq x \leq 0.4$ and then decrease gradually with increasing x in $0.4 \leq x \leq 1.0$. This sudden change in the isomer shift appears to accompany the transition from antiferromagnetic (or ferromagnetic) to paramagnetic behavior as mentioned above.

Isomer shift in iron compounds indicates a correlation between the IS and the valence state of the iron (*15*). The MS of $Sr_xLa_{1-x}FeO_3$ with $x = 0.7$–1.0 show a dominant peak at −0.20 to −0.10 mm/s and two small peaks at about 0.25 and 0.70 mm/s, respectively. These values are characteristic of Fe^{3+}_{oct} (0.35 mm/s) and Fe^{3+}_{tet}. The appearance of Fe^{3+}_{tet} can be correlated with the existence of two anionic vacancies in the vicinity of this iron and thus could be used to explain the vacancy distribution in perovskite in relation to the Brownmillerite-like structure ($ABO_{2.75}$). It is natural to conclude that the dominant peak corresponds to the Fe^{4+} state.

The MS of $Sr_xLa_{1-x}FeO_{3-\lambda}$, for $x = 0.4$, 0.5 each consist of a single broad and slightly asymmetric line with an IS (−0.04 mm/s) that lies between those of Fe^{3+} (0.25 mm/s) and Fe^{4+} (−0.15 mm/s). This value implies an average oxidation state for the iron and could be attributed to electron hopping either between Fe^{3+} and Fe^{4+} (*16*) or between Fe^{3+} and Fe^{5+} (*17*).

3. *Reaction between the Defect in Catalyst and the Oxygen Reactant*

In oxidative reactions the state of oxygen on the catalyst surface plays a key role in the reaction mechanisms and the distribution of reaction products (*18*). When oxidative reactions proceed on an oxide catalyst surface, a dynamic equilibrium among gaseous oxygen, adsorbed oxygen, and the bulk lattice oxygen could be envisioned as follows:

$$\begin{array}{ccccc} O_2\ (\text{gaseous}) & \rightleftharpoons & O_2\ (\text{physically adsorbed}) & \rightleftharpoons & O_2^-(\text{chemisorbed}) \\ & \searrow\!\!\uparrow & \downarrow\!\!\uparrow & \swarrow\!\!\nearrow & \\ & & O\ (\text{dissociative adsorption}) & \rightleftharpoons & O^{2-}(\text{oxygen ion adsorbed}) \\ & & & & \downarrow\!\!\uparrow \\ & & & & O^{2-}(\text{lattice oxygen ion}) \end{array}$$

In order to study the catalytic behavior of these series of catalysts in the oxidative reaction, information about the O_2 adsorbing capacity of the catalyst surface as well as the reactivity of the adsorbed oxygen should be obtained.

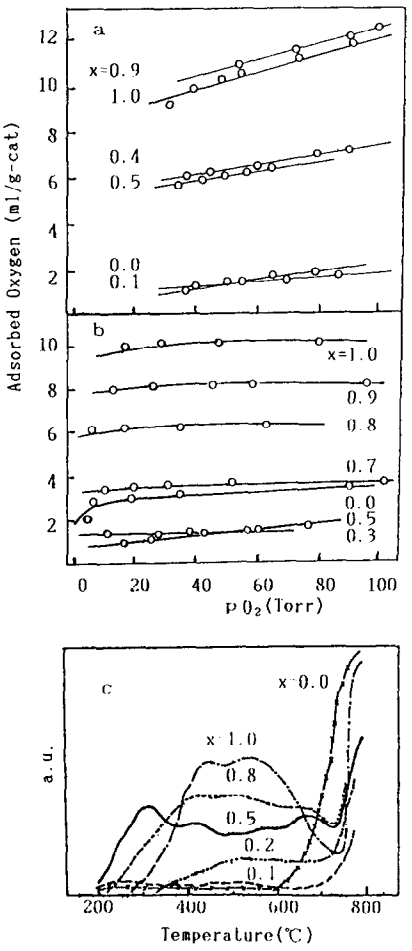

FIG. 17. Adsorption isotherm (600°C) of oxygen on (a) $Sr_xLa_{1-x}FeO_3$, (b) $Ca_xLa_{1-x}MnO_3$, and (c) TPD chromatogram on $Sr_xLa_{1-x}CoO_3$.

The oxygen adsorbed on different series of catalysts was measured by using the ordinary static method or TPD and is given in Tables 1(a)–(c) and Fig. 17a–c. Our results indicated that when temperature <700°C, the amount adsorbed (or released in TPD) increased with x, similar to the trend of λ variation. The general pattern shows that the oxygen adsorbing ability of catalyst surface closely follows the content of oxygen vacancies (λ) in the bulk; i.e., the more negative the nonstoichiometry, the more oxygen adsorbs on the catalyst.

XPS spectra of these series of catalysts provided convincing evidence for this inference (Fig. 18). Based on the electron binding energy of O_{1s}, which is about 530 eV for lattice oxygen, slightly lower than that for chemically adsorbed oxygen (532 eV), the XPS spectrum for ABO_3 showed that lattice oxygen predominates over adsorbed oxygen. On the contrary, the XPS spectrum obtained from $A'ABO_3$ showed that adsorbed oxygen is superior, its peak almost covering that of lattice oxygen. After a catalyst (e.g., $Ca_{0.8}La_{0.2}MnO_3$, in which adsorbed oxygen is superior) was etched with argon for 10 min, its XPS spectrum showed a decrease for the peak 532 eV clearly. This fact proved further that the peak 532 eV is surely that of adsorbed oxygen, and that oxygen adsorption increases with increasing a number of oxygen vacancies.

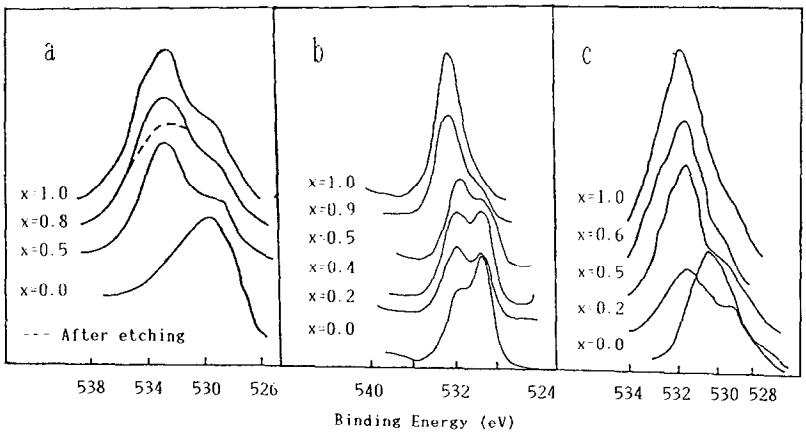

FIG. 18. O_{1s} XPS spectra of (a) $Ca_xLa_{1-x}MnO_3$, (b) $Sr_xLa_{1-x}FeO_3$, and (c) $Sr_xLa_{1-x}CoO_3$.

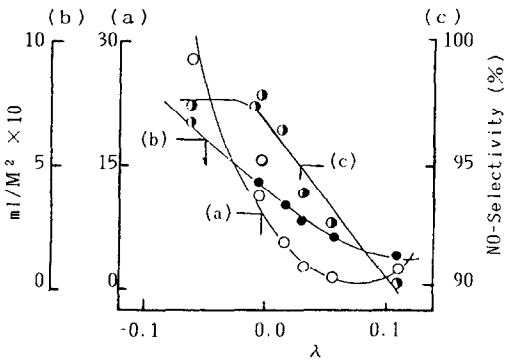

FIG. 19. Plots of (a) irreversible adsorbed oxygen, (b) surface excess oxygen, and (c) NO selectivity against nonstoichiometric oxygen (λ).

4. *Activity of Catalyst and the Possible Reaction Route*

There are three main reactions in the oxidation of ammonia on solid catalysts:

$$2\ NH_3 + 1.5\ O_2 \rightarrow N_2 + 3\ H_2O \quad (7)$$

$$2\ NH_3 + 2\ O_2 \rightarrow N_2O + 3\ H_2O \quad (8)$$

$$2\ NH_3 + 2.5\ O_2 \rightarrow 2\ NO + 3\ H_2O. \quad (9)$$

At fairly high temperatures (700–900°C), with either metal or oxide catalysts, the products are mainly NO and a trace of N_2. Therefore, NO selectivity is generally used for the evaluation of catalysts. We have measured the activity of these series of perovskite-type catalysts for ammonia oxidation. The catalytic selectivities at 700–800°C were in the order

$$A'_xA_{1-x}CoO_3 > A'_xA_{1-x}MnO_3 \gg A'_xA_{1-x}FeO_3.$$

In the case of the Mn system, the NO selectivity at 800°C tracked with λ in the same way as adsorbed oxygen and surface excess oxygen (Fig. 19). Thus there seems to be a direct interrelation between catalyst activity and the surface oxygen concentration. Therefore, the direct interaction between adsorbed oxygen and ammonia should be the second step of the reaction, and then after some intermediate steps, the products NO and N_2 would finally be formed. The possible reaction route may be

$$NH_3 + O_2^- \rightarrow NHO + H_2O + \boxed{e} \quad (10a)$$

$$NH_3 + O^- \rightarrow NH + H_2O + \boxed{e} \quad (10b)$$

$$NH + O^- \rightarrow NHO + \boxed{e} \quad (10c)$$

$$2\ NHO + O^- \rightarrow 2\ NO + H_2O + \boxed{e} \quad (10d)$$

$$NHO + NH \rightarrow N_2 + H_2O. \quad (10e)$$

The possibility of formation of O_2^- or O^- species was also tested by measuring the ESR of adsorbed oxygen on $Ca_{0.8}La_{0.2}Mn_{0.001}O_{1.1}$ catalysts in which Mn had been diluted. Figure 20 shows the hyperfine structure diagram of the ESR signal related to the interaction of unpaired electron with $I = \frac{5}{2}$ nuclear spinning. After adsorption of oxygen on the catalyst, a new signal appeared at the center of the hyperfine structure, $g = 2.007$, showing the paramagnetic property of adsorbed oxygen (Fig. 20b). In light of the electronic structure of oxygen, this signal is most probably due to O_2^- or O^-.

Having operated over 2500 h at 700–800°C, on scale-up installation, $Ca_{0.8}La_{0.2}$

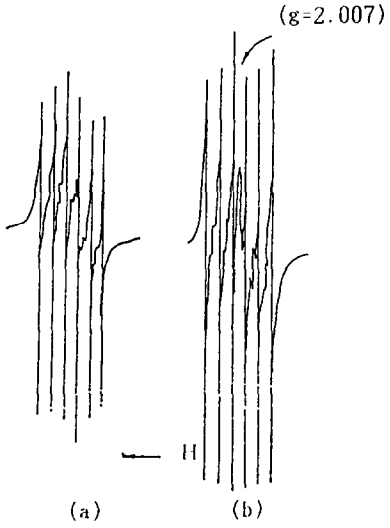

FIG. 20. Resolution of the weak Mn^{2+} ESR spectrum of $Ca_{0.8}La_{0.2}Mn_{0.001}O_{1.1}$ (a) before adsorption, pretreated at 650°C, measured at 293 K; (b) after adsorption, pretreated at 650°C and P_{O_2} = 10 Torr, measured at 77 K.

TABLE 5

Composition, Mn^{4+}-content, and Value of Nonstoichiometric Oxygen (λ) of a Catalyst Before and After Use

	Composition x	NO selectivity (%)	λ	Mn^{4+} (%)	Ads. O_2 (ml/g)
Before use	$x = 0.8$	97.0	0.010	82.50	2.73
After use	$x = 0.8$	95.0	0.012	82.55	3.69

MnO_3 has no marked change in catalyst composition, Mn valence state, or nonstoichiometric amount of oxygen (Table 5). It is concluded that neither the type or concentration of the defect could be changed distinctly. Hence it is believed that the lattice oxygen in these oxide catalysts would not take part in the reaction directly, or the process O^{2-} (adsorbed oxygen ion) $\rightleftharpoons$ O^{2-} (lattice oxygen ion) would attain equilibrium quite easily and is not a controlling step for the reaction. The role of the catalyst is the same as that of a metallic catalyst such as platinum or platinum–rhodium gauze. The main function of this type of catalyst is to provide an active site for activation of reactant oxygen; therefore, the reaction should be of a superfacial type.

The selectivity for NH_3 oxidation to NO at 700°C and the correlation between the content of Co^{3+} in the bulk and nonstoichiometry (λ) are shown in Fig. 21. It is noteworthy that the trend of NO selectivity

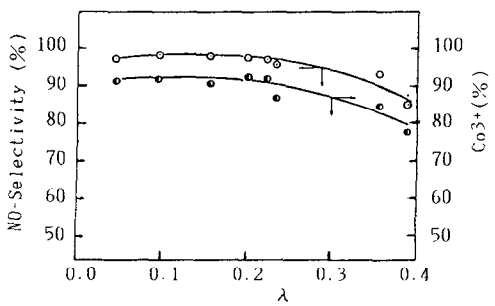

FIG. 21. Relationships among nonstoichiometric oxygen (λ), Co^{3+} content, and NO selectivity of $Sr_xLa_{1-x}CoO_3$.

variation is basically the same as that of Co^{3+} content in the bulk. This is reasonable, if one considers that the Co^{3+} is the active site during the reaction.

A mechanism for NH_3 oxidation over $A'_xA_{1-x}CoO_3$ was suggested as follows:

(a) The reaction proceeds via oxygen adsorption on Co^3 sites:

$$O_2 + Co^{3+} \rightarrow Co^{4+} + O_2^- \quad (11a)$$

$$O_2^- + Co^{3+} \rightarrow Co^{4+} + 2\,O^-. \quad (11b)$$

(b) The activated oxygen directly reacts with NH_3, and finally forms the products NO and N_2 through several intermediate steps:

$$NH_3 + O_2^- \rightarrow NHO + H_2O + \boxed{e} \quad (11c)$$

$$NH_3 + O^- \rightarrow NH + H_2O + \boxed{e} \quad (11d)$$

$$NH + O^- \rightarrow NHO + \boxed{e} \quad (11e)$$

$$2\,NHO + O^- \rightarrow 2\,NO + H_2O + \boxed{e} \quad (11f)$$

$$NHO + NH \rightarrow N_2 + H_2O. \quad (11g)$$

(c) Co^{4+} is reduced to Co^{3+} by lattice oxygen:

$$2\,Co^{4+} + O^{2-} \rightarrow 2\,Co^{3+} + \tfrac{1}{2}O_2(g) + Vo \quad (12a)$$

$$\tfrac{1}{2}O_2(g) + 2\,e^- \rightarrow O^{2-}. \quad (12b)$$

Thus, if the concentration of Co^{4+} were increased, the selectivity of the catalyst would decrease, which coincides well with experimental results.

The thermal stability of $Sr_{0.2}La_{0.8}CoO_3$, which is representative of the series of $Sr_xLa_{1-x}CoO_3$, was higher than that of Co Co_2O_4 (spinel) during NH_3 oxidation. The reaction proceeded at 900°C for 24 h. The result is shown in Fig. 22. The activity of the $Sr_{0.2}La_{0.8}CoO_3$ catalyst does not distinctly change and is higher than that of the $CoCo_2O_4$, but the activity of the $CoCo_2O_4$ decreases as time goes on.

The Fe system resembled neither the Mn system nor the Co system, as shown in Fig. 23. The catalytic activity achieves a maxi-

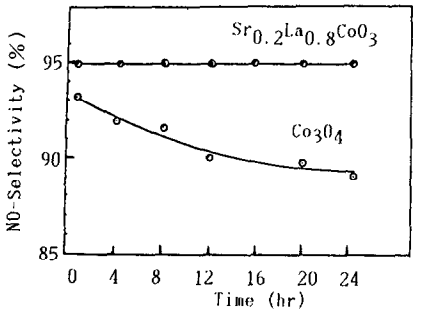

FIG. 22. Thermal stability of different catalysts.

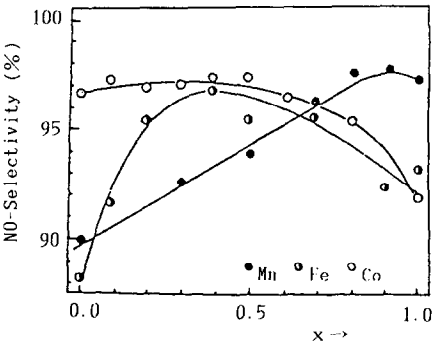

FIG. 24. Relationships between NO selectivity and x of $A'_xA_{1-x}BO_3$ (B = Mn, Fe, Co).

mum at $x = 0.4$ and seems neither simply dependent on the concentration of metallic ion (Fe^{3+} or Fe^{4+}) nor on the amount of adsorbed oxygen (or λ). When the variation of selectivity of all three systems with respect to x is plotted on the same coordinates (Fig. 24), the Fe system is seen to lie between the Co and Mn systems.

From the relationships between catalytic activity and other factors of Mn and Co systems, we could deduce that the catalytic activity of $A'_xA_{1-x}BO_3$ mixed oxide in the NH_3 oxidation, in general, could be attributed to the extent of the redox reaction

$$2\,B^{4+} + O^{2-} \underset{\text{Mn}}{\overset{\text{Co}}{\rightleftharpoons}} 2\,B^{3+} + \tfrac{1}{2}O_2(g) + \text{Vo}. \qquad (13)$$

It indicates that the forward reaction is favored for Co, and the reverse for Mn.

From Eq. (13), it could be predicted, and has been obtained from our experiments, that samples containing more B^{4+} and Vo for the Mn system but less B^{4+} and Vo for the Co system are the most active. Moreover, the trends in variation of B^{4+} and λ in the Fe and Mn systems (Fig. 24) are in parallel to each other, but the relation for the corresponding parameters is just the reverse. This means that the oxidation reaction of Eq. (13) takes place with more difficulty in the Fe system than that in the Mn system. By comparing the curves referring to the Fe and Co systems, we deduce that the reduction of the Fe system is more difficult than that of the Co system. Based on this point of view, the catalytic activity of Fe-containing mixed oxides should also depend on the redox ability of this system. Our results obtained from TPR measurement and ^{18}O-isotopic exchange investiga-

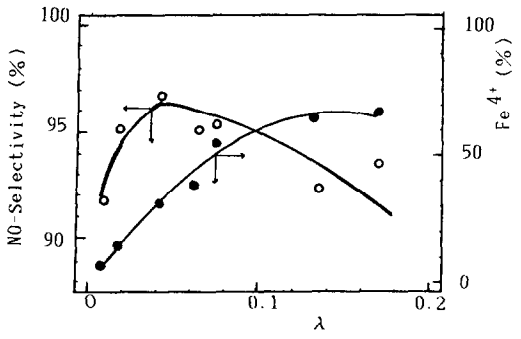

FIG. 23. Relationships among Fe^{4+} content, nonstoichiometry (λ), and NO selectivity.

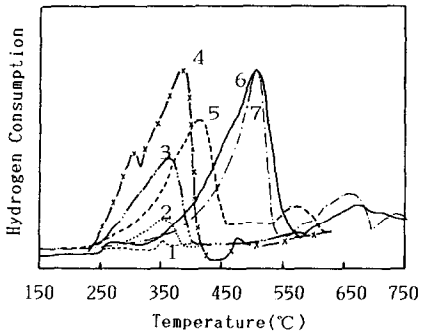

FIG. 25. TPR profiles for $Sr_xLa_{1-x}FeO_3$: (1) $x = 0.0$; (2) $x = 0.2$; (3) $x = 0.4$; (4) $x = 0.5$; (5) $x = 0.7$; (6) $x = 0.9$; (7) $x = 1.0$.

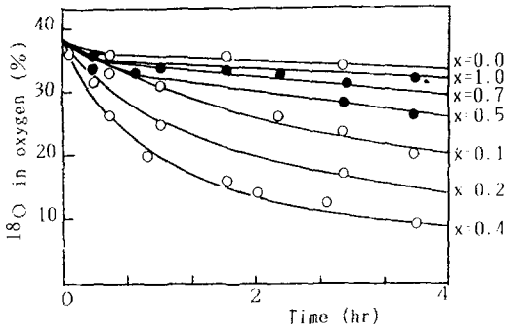

FIG. 26. Isotopic exchange of oxygen over $Sr_xLa_{1-x}FeO_3$ at 400°C.

tion of this series of catalysts have provided information about the reducibility as well as the ^{18}O-isotopic exchange ability, as shown in Figs. 25 and 26. Catalysts possessing maximum activity are related in that both are more easily reduced and more active toward ^{18}O-isotopic exchange. In short, for the Fe system the reducibility as well as the ^{18}O-isotopic exchange ability also vary in parallel with the catalytic activity.

REFERENCES

1. William, R., and Halpern, J. (Eds.), "Catalytic Materials on Solid State Inorganics." New York Acad. Sciences, New York, 1976.
2. (*a*) Grenier, J. C., Pouchard, M., and Paul, H., *Struct. Bonding* (Berlin) **47,** 1–25 (1981); Rao, N. R., Gopalakrichman, J., and Vidyasagar, K., *Indian J. Chem. Sect. A* **23,** 265 (1984); (*b*) Bevan, D. J. M., "Non-stoichiometric Compounds in Comprehensive Inorganic Chemistry," p. 453. Pergamon, Elmsford, NY, 1973.
3. Grasselli, R. K., and Brazdil, J. F. (Eds.), "Solid State Chemistry in Catalysis," ACS Symposium Series, Vol. 279. *Amer. Chem. Soc.*, Washington, D.C., 1985.
4. Uehijima, T., Takahashi, M., and Yoneda, Y., *J. Catal.* **9,** 403 (1967).
5. Cvetanovic, R. J., and Amenomiya, Y., *in* "Advances in Catalysis" (D. D. Eley, H. Pines, and P. B. Weisz, Eds.), Vol. 17, p. 107. Academic Press, New York, 1967.
6. Kamata, K., Nakajima, T., Hayashi, T., and Nakamura, T., *Mater. Res. Bull.* **13**(1), 49 (1978).
7. For example: Ohbayashi, H., Kudo, T., and Gejo, T., *Japan J. Appl. Phys.* **13** (1), 1 (1974); Takano, M., Kawachi, J., Nakanishi, N., and Takeda, Y., *J. Solid State Chem.* **39,** 75 (1981); Misono, M., and Nitador, T., *in* "Adsorption and Catalysts on Oxide Surface (M. Che and G. C. Borle, Eds.). Elsevier, Amsterdam, 1985.
8. Wolfram, T., Kraut, E. A., and Morin, F. J., *J. Phys. Rev. B* **7,** 167 (1973).
9. Tofield, B. C., and Scott, W. R., *J. Solid State Chem.* **10,** 183 (1974).
10. Wold, A., and Arnott, R. J., *J. Phys. Chem. Solids* **9,** 176 (1959).
11. Solymosi, F., "Contact Catalysis" (Z. G. Szabo and D. Kallo, Eds.), Vol. 1, pp. 86–124. Elsevier, Amsterdam, 1976.
12. Vallet-Regi, M., Gonzalez-Calbet, J., Alario-Franco, M. A., Grenier, J. C., and Hagenmuller, P., *J. Solid State Chem.* **55,** 251 (1984).
13. Gonzalez-Calbet, J. M., Vallet-Regi, M., Alario-Franco, M. A., and Grenier, J. C., *Mater. Res. Bull.* **18,** 285 (1983); Takeda, Y., Kanno, K., Takada, T., Yamamoto, O., Takano, M., Nakayama, N., and Bando, Y., *J. Solid State Chem.* **63,** 237 (1986); Tofield, B. C., Greaves, C., and Fender, B. E. F., *Mater. Res. Bull.* **10,** 737 (1975).
14. Reller, A., and Bunsenges, B., *Phys. Chem.* **90,** 742 (1986).
15. Rodriguez, J., Pereda, J. A., Vallet, M., Calbet, J. G., and Tejada, J., *Mater. Res. Bull.* **21,** 255 (1986).
16. Shimony, U., and Knudsen, J. M., *Phys. Rev.* **144,** 361 (1966).
17. Takano, M., and Takeda, Y., *Bull. Inst. Chem. Res. Kyoto Univ.* **61**(5–6), 4 (1983).
18. Moro-oka, Y., *Shokubai.* **21**(1), 7 (1979).